Energy & Environmental Science

3D Porous Graphitic Nanocarbon for Enhancing Performance and Durability of Pt Catalysts: Balance between Graphitization and Hierarchical Porosity

Journal:	*Energy & Environmental Science*
Manuscript ID	EE-ART-06-2019-001899
Article Type:	Paper
Date Submitted by the Author:	14-Jun-2019
Complete List of Authors:	Qiao, Zhi; University at Buffalo - The State University of New York, Chemical Engineering Hwang, Sooyeon; Brookhaven National Laboratory, Center for Functional Nanomaterials Li, Xing ; Brookhaven National Laboratory, Center for Functional Nanomaterials Wang , Chengyu; Los Alamos National Laboratory Samarakoon, Widitha; Oregon State University, School of Chemical, Biological, and Environmental Engineering Karakalos, Stavros; University of South Carolina, College of Engineering and Computing Li, Dongguo; Los Alamos National Laboratory Chen, Mengjie; University at Buffalo, SUNY, Chemical and Biological Engineering He, Yanghua; University at Buffalo, SUNY, Chemical and Biological Engineering Wang , Maoyu; Oregon State University, School of Chemical, Biological, and Environmental Engineering Liu, Zhenyu; Universiy of Pittsburgh, Zhou, Hua; Argonne National Lab, Advanced Photon Source Wang, Guofeng; Univeristy of Pittsburgh, Mechanical Engineering and Materials Science Feng, Zhenxing; Oregon State University, School of Chemical, Biological, and Environmental Engineering; Su, Dong; Brookhaven National Laboratory, Center for Functional Nanomaterials Spendelow, Jacob; Los Alamos National Laboratory, Wu, Gang; University at Buffalo, SUNY, Chemical and Biological Engineering

Broader Context

Proton exchange membrane fuel cells (PEMFCs) have been considered an ideal power source for electric vehicles. Highly durable and active cathode catalysts are highly demanded for full commercialization to boost the sluggish oxygen reduction reaction (ORR). State-of-the-art catalysts are Pt and Pt alloy nanoparticles dispersed on porous carbon supports to improve catalyst utilization and mass transfer. However, current carbon supports suffer from significant corrosion under the practical operation conditions of PEMFCs, causing serious performance degradation. This carbon corrosion therefore is largely responsible for insufficient durability of current fuel cells and become a critical limitation. Due to the highly-ordering feature, highly graphitized carbon materials are more stable, however, they usually lead to the low surface area and insufficient porosity, which make them unfavorable for mass transfer and ionomer dispersion in cathodes. This work reports a new class porous graphitic carbon (PGC) with optimal balance between graphitization and porosity, which is derived from polymer hydrogels through a carbonization at a relatively low heating temperature catalyzed by manganese salts. The PGC supported Pt catalysts achieved dramatically enhanced performance durability in PEMFCs, representing the most promising carbon support candidate for the clean and high-efficient fuel cell technologies for transportation applications.

ARTICLE

3D Porous Graphitic Nanocarbon for Enhancing Performance and Durability of Pt Catalysts: Balance between Graphitization and Hierarchical Porosity

Received 00th January 20xx,
Accepted 00th January 20xx

DOI: 10.1039/x0xx00000x

Zhi Qiao[a,1], Sooyeon Hwang[b,1], Xing Li[b,h1] Chenyu Wang[c,1], Widitha Samarakoon[d], Stavros Karakalos[e], Dongguo Li[c], Mengjie Chen[a], Yanghua He[a], Maoyu Wang[d], Zhenyu Liu[g], Guofeng Wang[g], Hua Zhou[f], Zhenxing Feng *[d], Dong Su*[b], Jacob S. Spendelow*[c] and Gang Wu*[a]

Carbon supports used in oxygen-reduction cathode catalysts for proton exchange membrane fuel cells (PEMFCs) are vulnerable to corrosion under harsh operating conditions, leading to poor performance durability. To address this issue, we have developed a highly stable porous graphitic carbon (PGC) produced through pyrolysis of a 3D polymer hydrogel in combination with Mn. The resulting PGC features multilayer carbon sheets assembled in porous and flower-like morphologies. In-situ high-temperature electron microscopy was employed to dynamically monitor the carbonization process up to 1100°C, suggesting that 3D polymer hydrogel provides high porosity at multiple scales, and that Mn catalyzes the graphitization process more effectively than other metals. Compared to conventional carbons such as Vulcan, Ketjenblack, and graphitized carbon, the PGC provides an improved balance between high graphitization and hierachical porosity, which is favorable for uniform Pt nanoparticle dispersion and enhanced corrosion resistance. As a result, Pt supported on PGC exhibits remarkably enhanced stability. In addition to thorough testing in aqueous electrolytes, we also conducted fuel cell testing using durability protocols recommended by the U.S. Department of Energy (DOE). After 5000 voltage cycles from 1.0 to 1.5 V, the Pt/PGC catalyst only lost 9 mV at a current density of 1.5 A/cm^2, dramatically exceeding the DOE support durability target (<30 mV), and surpassing commercial Pt/C catalysts. Along with the enhanced carbon corrosion resistance of the PGC support, the enhanced catalyst-support interactions are beneficial for stability improvement, likely due to nitrogen doping into carbon, which was further elucidated through X-ray absorption spectroscopy and density functional theory (DFT) calculations. Thus, the high stability and activity of PGC-based Pt catalysts are attributed to the combination of high graphitization degree, favorable surface areas and porosity, and nitrogen doping, which effectively stabilize highly dispersed Pt nanoparticles.

1. Introduction

Proton exchange membrane fuel cells (PEMFCs) have attracted substantial attention because of their high energy efficiency and environmental friendliness. Impressive progress has been achieved during recent years, but improvements in several components, especially catalysts for cathode, are still needed to meet the cost and durability targets for large-scale fuel cell commercialization. State of the art catalysts are based on Pt and Pt alloy nanoparticles dispersed on high-surface area carbon supports, which are able to stabilize the nanoparticles to increase catalyst utilization and provide effective mass transport and electronic conductivity. However, catalyst durability with low Pt loadings remains insufficient for practical applications due to the existences of several degradation mechanisms. Poor support stability, which leads to the detachment of Pt nanoparticles, particle agglomeration, and the compaction and then the loss of electrode porosity, is a critical limitation on durability of current catalysts. A variety of conductive materials have been studied as the support for Pt, including nanostructured carbons, conductive diamonds, conductive oxides and carbides.[1] Among them, nanostructured carbon materials have been the most successful due to their high surface area, high electrical conductivity, good interaction with Pt, and reasonable stability in acidic media.[2] Currently, XC-72 and Ketjen black are among the most promising supports, and are commercially used for Pt/C catalysts. However, as amorphous carbon materials with low degree of graphitization, they are not electrochemically stable under the corrosive conditions in PEMFCs, which include high oxygen concentration, high water content, low pH, elevated temperature up to 100°C, and high electrode potential. Thus, severe carbon corrosion has been observed in fuel cell catalysts, leading to unacceptable catalyst durability.[3]

[a.] Department of Chemical and Biological Engineering, University at Buffalo, The State University of New York, Buffalo, New York 14260, United States. E-mail: gangwu@buffalo.edu
[b.] Center for Functional Nanomaterials, Brookhaven National Laboratory, Upton, New York 11973, United States. Email: dsu@bnl.gov
[c.] Materials Physics and Applications Division, Los Alamos National Laboratory, Los Alamos, New Mexico 87545, United States. Email: spendelow@lanl.gov
[d.] School of Chemical, Biological, and Environmental Engineering, Oregon State University, Corvallis, Oregon 97333, United States. Email: zhenxing.feng@oregonstate.edu
[e.] Department of Chemical Engineering, University of South Carolina, Columbia, South Carolina 29208, United States
[f.] X-ray Science Division, Argonne National Laboratory, Argonne, Illinois 60439, United States
[g.] Department of Mechanical Engineering and Materials Science, University of Pittsburgh, Pittsburgh, PA 15261, United States
[h.] Department of Physics and Engineering, Key Laboratory of Material Physics, Zhengzhou University, Zhengzhou, 450052, China
1. These authors contributed equally.
Electronic Supplementary Information (ESI) available: See DOI:10.1039/x0xx00000x

To address this considerable challenge, many kinds of carbon materials have been investigated as catalyst supports, and it has been observed that structural properties of carbon, such as the degree of graphitization, morphology, and surface area, can have a significant effect on the catalytic activity and durability.[4-6] Among them, carbon nanotubes and carbon nanofibers (CNTs and CNFs) with high graphitization attracted attention in recent years, and improved activity and stability have been claimed.[7-9] However, due to the limitation of specific surface area and porous structure, the electrochemical surface area of Pt could be restricted in the case of CNTs and CNFs, which could limit the catalytic performance in a fuel cell.[10] Although enhanced stability was observed in aqueous acidic electrolytes, poor dispersion of Nafion ionomer in CNT supported Pt cathodes usually leads to poor fuel cell performance, especially at high current density.[11] Another candidate support is graphitized carbon, which has been suggested to be more favorable in terms of the decrease of electrical resistance and enhancement of carbon corrosion resistance. Unfortunately, most graphitization approaches compromise the porosity and specific surface area of carbon, while also weakening interactions between carbon and platinum, making it difficult to uniformly disperse Pt nanoparticles on the support. Therefore, significant challenges still remain to develop advanced support materials for Pt catalysts in future PEM fuel cells.

Herein, we report a highly durable and active Pt catalyst supported on a three-dimensional (3D) porous graphitic carbon (PGC) derived from polymer hydrogel. Hydrogel, consisting of a 3D network of crosslinked polymer chains containing large amounts of water, has been extensively studied as a carbon precursor.[12-14] Hydrogel precursors yield porous support architectures, which could provide improvements in active site density, mass/charge transfer, and structural integrity.[15-17] The polymers selected to prepare hydrogel in this work are crosslinked polyaniline (PANI) and polypyrrole (PPy), which have been proved to be effective nitrogen/carbon precursors for catalysts.[18-20] In particular, PANI is rich in aromatic structures similar to graphitized carbon, and abundant carbon and nitrogen sources help direct conversion to graphitized carbon.[18, 21] By adding pyrrole, highly folded and contorted graphitic structures with high uniformity and porosity can be produced from PANI-PPy composite.[22] In this work, PANI-PPy hydrogel composite was used to facilitate increased nitrogen doping in the resulting PGC, which is believed to provide significant improvements of activity and stability for Pt/C catalysts.[23-25] In addition, we introduced metal precursors including Fe, Co, Ni, or Mn into the polymerization process to take advantage of metal-catalyzed graphitization.[26] Among these metals, Mn is the most suitable for fuel cell applications since it does not cause degradation processes associated with the Fenton reactions.[27, 28] At the same time, Mn was demonstrated to be an effective catalyst for graphitization of polymer-derived carbon.[29, 30] Whereas conventional high temperature treatment requires temperatures up to 3000°C to produce highly graphitized carbon[31], the Mn-assisted hydrogel method is able to achieve a high degree of graphitization at only 1100°C, making this method attractive from a manufacturing standpoint.

Deposition of Pt nanoparticles onto the hydrogel-derived PGC resulted in a catalyst with dramatically enhanced electrochemical stability compared to commercial Pt/C catalysts, including TEC10V20E (Vulcan support), TEC10EA20E (graphitized carbon support) and TEC10E20E (high-surface-area carbon black). To the best of our knowledge, this is the first time that such highly graphitized and porous carbon has demonstrated such exceptional stability and performance under real fuel cell operating conditions. These PGCs may finally resolve the carbon corrosion issues that have limited widespread deployment of PEMFCs and other electrochemical technologies.

2. Results and discussion

2.1 Synthesis, structure, and morphology of PGC supports and Pt catalysts

The polymer hydrogel approach to preparing PGC supports is illustrated in **Figure 1a**. During the synthesis, ammonium persulfate was applied as an initiator for the polymerization of aniline and pyrrole to produce highly crosslinked and folded polymer nanostructures. After removing water from the hydrogel precursor, the first heat treatment was applied to fully carbonize precursors to highly graphitized carbon with the assistance of manganese. In order to purify the carbon, acid leaching was used to remove metal aggregates in the resulting carbon structure. A second heat treatment was used to further stabilize and reconstruct the carbon by removing oxygen containing functional groups formed during acid leaching. SEM images shown in **Figure S1** provide a comparison of different hydrogel-Mn precursors (PANI *vs*. PANI+PPy) and their corresponding carbon. During the transition from precursors to carbon supports, the 3D porous structure was well maintained and became even more open. After adding pyrrole, the diameter of the short fibers increased and the structure became more disordered. This highly porous morphology is crucial for providing enough surface area for depositing Pt nanoparticles. TEM and STEM images shown in **Figures 1b** and **c** demonstrate that flower-like graphitic carbon structures with high irregularity are apparent in PGCs derived from the individual PANI and the binary PANI+PPy, respectively. Compared to the Mn-PANI precursor-derived carbon, the one from Mn-PANI-PPy exhibits thicker carbon layers folded irregularly, indicating a higher graphitic carbon content and higher porosity.

To study the carbon structure and the degree of graphitization, Raman spectra for relevant carbon samples are compared in **Figure 2a**. Peak fitting was performed following the procedure outlined in previous literature.[16, 32, 33] The peak intensity ratio ($I_{(D)}/I_{(G)}$) of the D (~1350 cm^{-1}) and G (~1590 cm^{-1}) bands was chosen to determine the degree of graphitization, with lower values of $I_{(D)}/I_{(G)}$ indicating a higher degree of

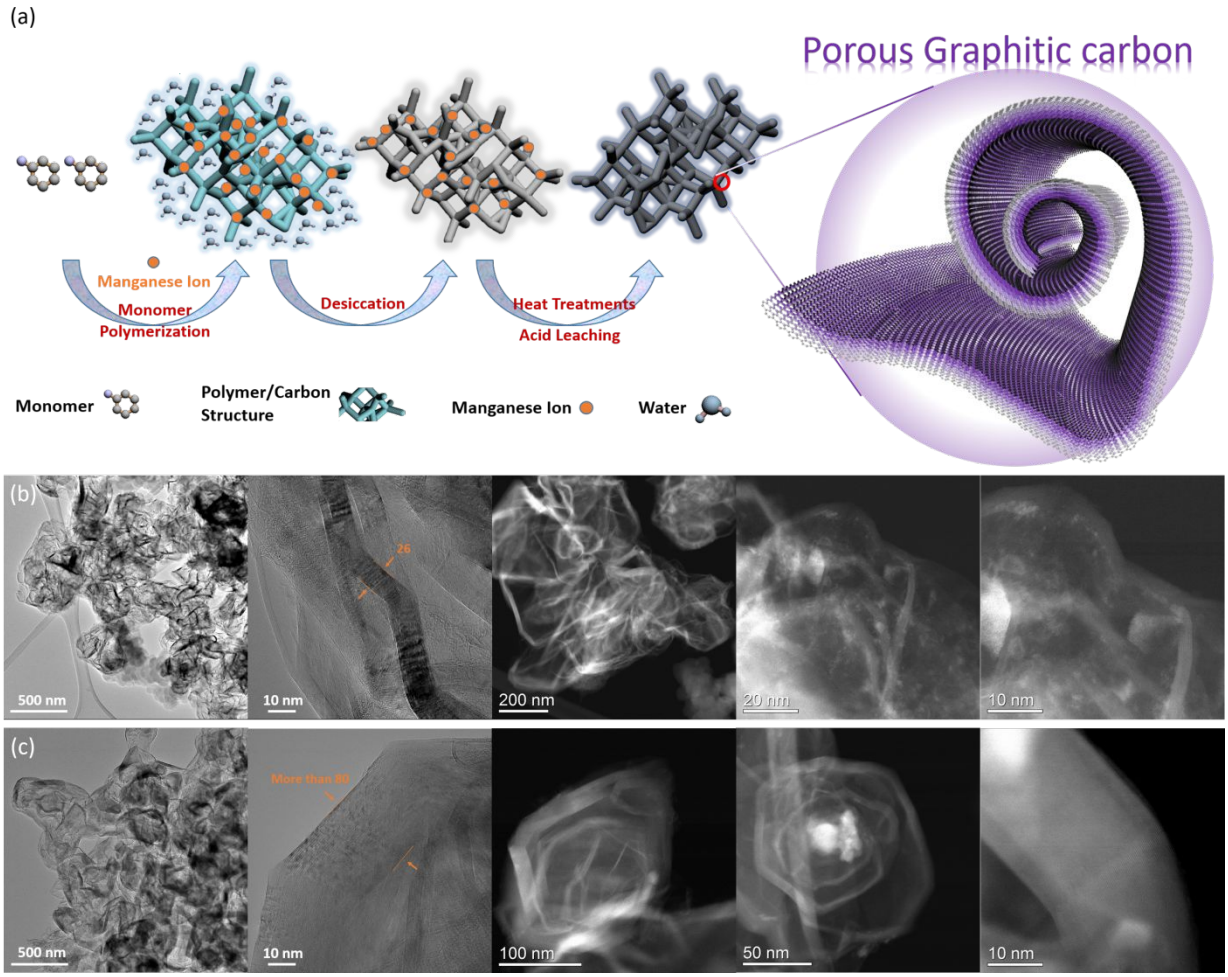

Figure 1. (a) Synthesis scheme for porous graphitic carbons (PGCs) derived from polymer hydrogel; TEM, HRTEM and STEM images of **(b)** Mn-PANI-PGC and **(c)** Mn-PANI-PPy-PGC at different magnifications.

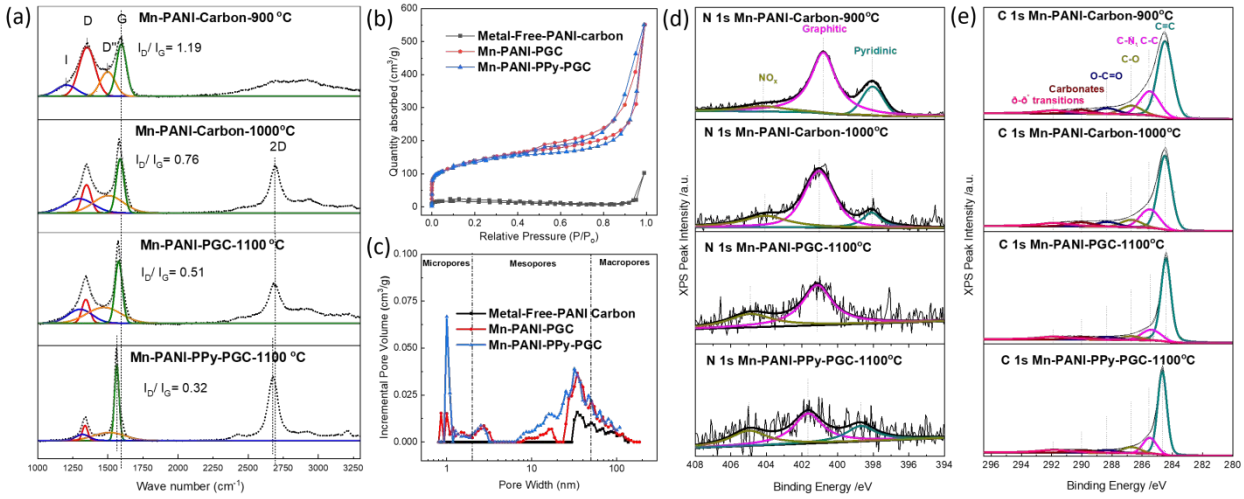

Figure 2. (a) Raman spectra, **(b)** N_2 adsorption/desorption plots, **(c)** corresponding pore size distributions, and high-resolution XPS **(d)** N1s, **(e)** C1s spectra for PGCs synthesized at different temperatures.

graphitization.[34] It is apparent that higher heating temperature leads to decreased value of $I_{(D)}/I_{(G)}$, indicating increased degree of graphitization. At the same heating temperature of 1100°C, addition of PPy is able to further increase the degree of graphitization, as evidenced by decreased $I_{(D)}/I_{(G)}$ of 0.32 and more separated D and G peaks when compared to that of individual PANI-derived carbon. A continuous shifting of G peak from 1596 to 1563 cm^{-1} was observed when the heating

temperature was increased from 900 to 1100°C. According to previous widely accepted knowledge,[35-37] this is evidence for decreased doping level and defect density, which is in accordance with increased graphitization degree. In addition to D and G bands, the I band observed at a wide range (~1180–1290 cm^{-1}) and the D" band at ~1500 cm^{-1} are indications of the disorder in the graphitic lattice and the presence of amorphous carbon, respectively.[38, 39] The nearly vanished I and D" peaks in the case of Mn-PANI-PPy-PGC-1100 carbon are also indicative of the further improved graphitization degree. Also, the second order of the D peak, noted as 2D peak, appeared when the heating temperature increased higher than 1000°C, and becomes even sharper in the case of Mn-PANI-PPy-PGC-1100. This is further evidence of graphitic features.[40] For a comparison to Mn, we also evaluated carbon samples derived from PANI hydrogel combined with different metals including Fe, Co, or Ni, and the metal-free scenario. Their Raman spectra are shown in **Figure S2**. Only Mn-derived carbon has relatively sharp G and 2D peaks, indicating its significant advantages to achieve high graphitization degree. BET analysis (**Figure 2b** and **c**) was carried out to characterize the specific surface area and porosity of the hydrogel-derived PGCs. A very low surface area of 45 m^2/g was measured with the metal-free PANI hydrogel derived carbon. Addition of Mn into the hydrogel precursors provided an increase in surface area to 477 m^2/g with cumulative pore volume of 0.53 cm^3/g, which are more than 10 times higher than the metal-free hydrogel-derived carbon sample. Adding pyrrole to the precursors does not significantly change the surface area, which remains at 458 m^2/g. However, the cumulative pore volume increased substantially to 0.70 cm^3/g. This could be due to the short fiber structures with lower aspect ratios of PANI-PPy hydrogel, which leads to a highly folded morphology possessing more favorable porosity, especially mesopores. Both Mn-PANI and Mn-PANI-PPy derived PGCs have abundant pores at different sizes, but a higher volume of mesopores and micropores was only observed with the Mn-PANI-PPy-PGC. The pores in the PGCs are likely created by two mechanisms. One type of pore is due to the removal of Mn aggregates during acid leaching; the other is related to the highly folded carbon layer structures resulting from the porous hydrogel. In previous study, mesopores were found to be crucial as sites for Pt deposition with facile mass transport.[41] Thus, the higher mesoporosity of Mn-PANI-PPy-PGC makes it favorable as the support in Pt/C catalysts. The chemical states in surface layers of PGCs obtained at different heating temperatures were characterized by using XPS. Their corresponding N1s and C1s spectra are represented in **Figures 2d** and **e,** respectively. Three types of doped N atoms were observed in these PGCs, including pyridinic-N (398.4 eV) at edges of carbon planes, graphitic-N doped in the interior of the graphitic planes (401 eV), and oxidized pyridinic-N (404.8 eV) associated with oxygen. The absence of pyrrolic-N related to five-sided rings could be due to its instability at the elevated temperatures used in the synthesis

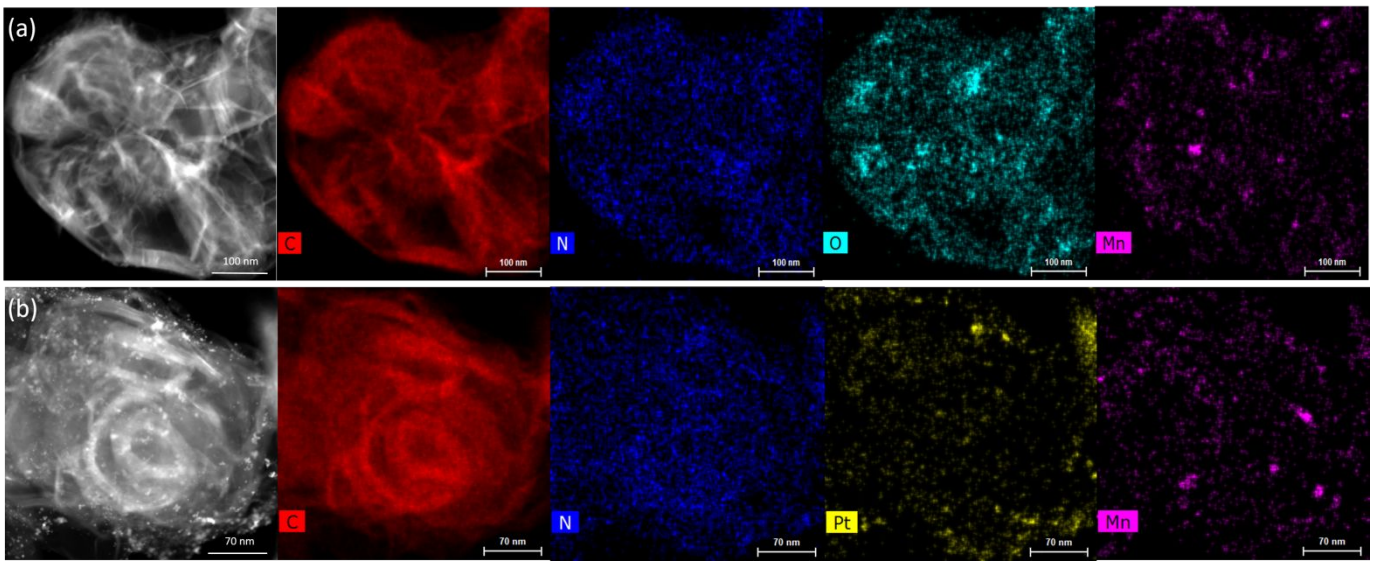

Figure 3. STEM-EDS elemental mapping of **(a)** Mn-PANI-PPy-PGC and **(b)** Pt catalysts supported on Mn-PANI-PPy-PGC.

(>800°C).[42-44] Pyridinic-N was a minor component in the PANI-Mn-PGC treated at 1100°C, which is in agreement with Raman in term of the decreased defect density. However, incorporation of PPy in the synthesis caused pyridinic-N to become apparent in PANI-PPy-Mn-PGC samples treated at 1100°C, which is one of the advantages of using binary PANI and PPy polymer hydrogel. Deconvolution of the high-resolution XPS C 1s peak revealed six different components due to the existence of various carbon moieties and π-π* interactions in the graphitic structure. With increasing temperature, more dominant and narrower peaks for C-C were observed, suggesting a higher degree of graphitization, which is consistent with Raman results. The Mn 2p spectra are also shown in **Figure S3**. Due to the low Mn content, the spectra are somewhat vague and only trace levels of MnO_x were observed. This suggests that most Mn was removed during the acid-leaching step and only

very low amounts remain in the graphitic structure, which is further confirmed by EDS mapping images in **Figure 3a**. The elemental quantification determined by XPS for these PGCs is summarized in **Table S1**, which shows only trace amounts of Mn in all the samples and decreased nitrogen content when the temperature of heat treatment was increased. In addition, uniform nitrogen doping was also confirmed by STEM-EDS mapping **(Figure 3a** and **Figure S4).** After depositing Pt nanoparticles on the PGCs, we applied a post annealing treatment to further remove unstable components and strengthen interactions between Pt and the PGC support. The TEM images shown in **Figure S5** demonstrated that most of the Pt nanoparticles are well dispersed on the Mn-PANI-PPy-PGC, which was further verified by using STEM-EDS elemental mapping **(Figures 3b)**.

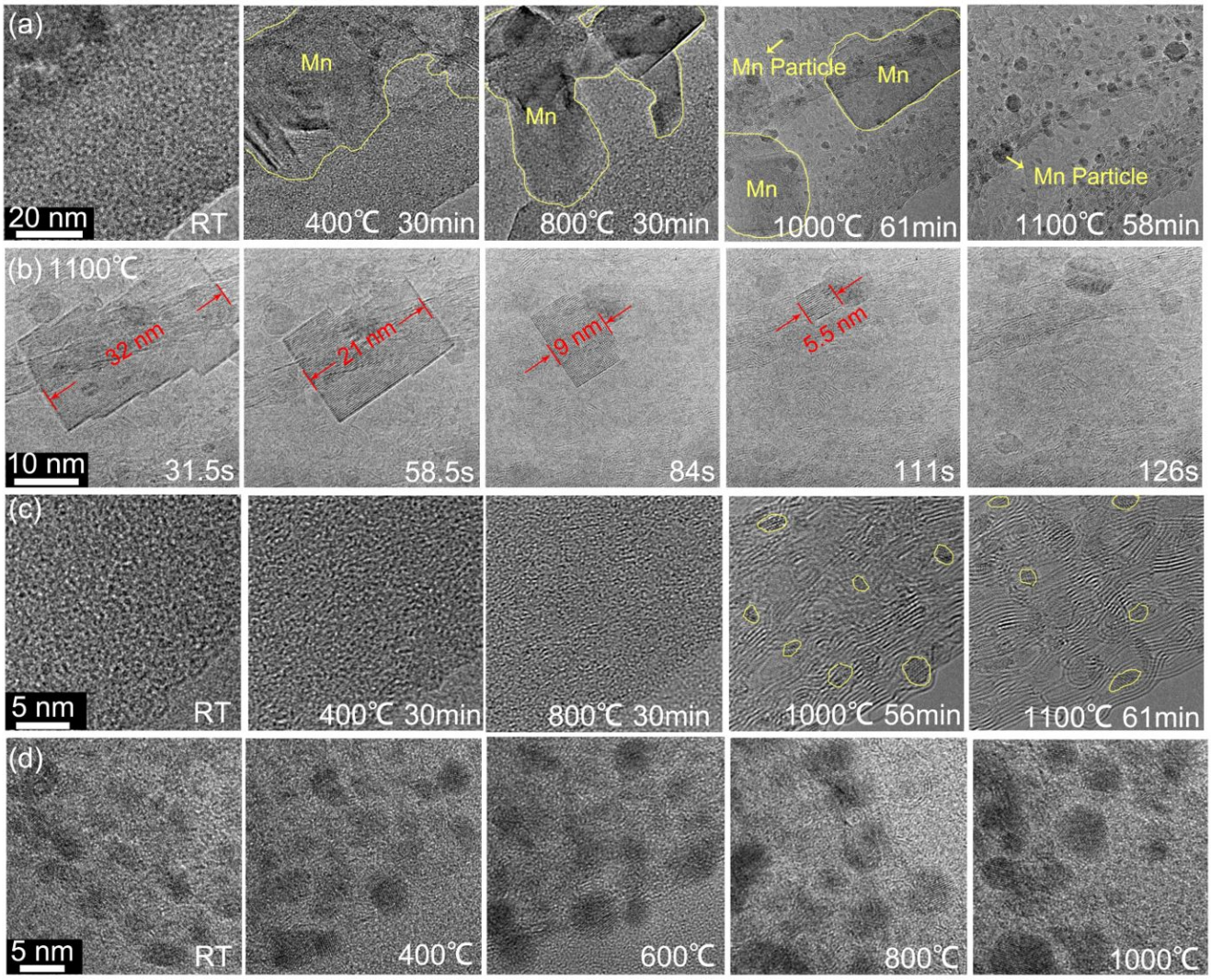

Figure 4. (a) In-situ TEM images showing the evolution of Mn species in the Mn-PANI-PPy precursor at RT, 400, 800, 1000, and 1100 °C. The regions of Mn species are highlighted by the yellow outlines. **(b)** In-situ HRTEM image series showing the sublimation process of a Mn particle at 1100 °C. In-situ HRTEM images **(c)** showing the evolution of carbon in Mn-PANI-PPy precursor at heating temperatures of RT, 400, 800, 1000, and 1100 °C (some crystalized Mn particles are highlighted by yellow outlines); **(d)** of Pt/Mn-PANI-PPy-PGC at pyrolysis temperatures of RT, 400, 600, 800, and 1000 °C.

Rose-like graphitic carbon nanostructures are dominant, which is in agreement with the morphology of PGC in STEM images **(Figure 1c)**. Nitrogen was found dispersed uniformly throughout the carbon, while Mn was detected sparsely, in agreement with XPS results. The XRD patterns for Pt nanoparticles deposited onto two different PGCs derived from PANI-Mn and PANI-PPy-Mn are shown in **Figure S6**. Both samples exhibited four diffraction peaks at 2θ = 39.76°, 46.24°, 67.45° and 81.41°, which are consistent with those of Pt metals with an fcc structure, corresponding to the (111), (200), (220) and (311) planes. No peak shifting was observed, indicating that negligible alloying with manganese occurred even during the post annealing treatment (**Figure S7**). The sharp peak observed in each sample at 2θ = 26.45° corresponds to the (002) diffraction of graphitic carbon, which provides further evidence for highly graphitic carbon structures in these Pt/PGC catalysts.

To dynamically study the evolution of Mn-PANI-PPy hydrogel from precursor to carbon material in real time, we carried out

in-situ HRTEM and STEM-EDS analysis and simulated the heat treatment conditions to monitor the carbonization process. **Figure 4a** shows the changing distribution of Mn during a gradual increase in temperatures up to 1100°C. At the room temperature, Mn species were found to be distributed evenly at the edge of samples and then gradually agglomerated after 30 min heating at 400°C. Recrystallization process of Mn species was observed when heating at 800°C and 1000°C. Along with the recrystallization process, crystallized Mn particles were observed well distributed in the carbon matrix. Importantly, as shown in **Figure 4b**, the large crystalized Mn particle with size of 32 nm was gradually decomposed in 126s at 1100°C. Finally, small crystallized Mn particles were uniformly dispersed in the carbon matrix. This evolution was also observed in EDS maps with different resolutions shown in **Figure S8**. This finding contrasts with previous studies of metal particle (e.g., Fe) movement,[45] in which the particles continue to enlarge with increased temperatures. The highly dispersed Mn species at 1100°C are involved in catalyzing the formation of graphitized carbon. In-situ HR-TEM images shown in **Figure 4c** illustrate the process through which graphitization occurred as the temperature was increased, with layered graphitic domains becoming apparent at 1000°C and 1100°C with uniformly districted crystallized Mn particles. In-situ HR-TEM images shown in **Figure S9** demonstrate that longer duration of pyrolysis results in more uniform Mn dispersion and increased graphitization. The Pt nanoparticles deposited onto the Mn-PANI-PPy-PGC support were also studied by using in-situ HRTEM to mimic the post annealing treatment, which was found to be a critical step in improving catalytic activity and stability. Average particle size increased from around 3 to 5 nm when the annealing temperature was increased to 1100°C (**Figure 4c**), which could help to stabilize the nanoparticles and reduce agglomeration.

2.2 Promotional role of N doping in strengthening metal-support interactions

The XPS N 1s and Pt 4f spectra are shown in **Figure 5a** and **b,** respectively, for Pt catalysts deposited onto Mn-PANI-PGC and Mn-PANI-PPy-PGC supports. The Pt 4f spectra show that Pt is primarily in the metallic state. In addition, a slight shift of the Pt 4f peaks to higher binding energy and a shift of the N 1s peaks toward lower binding energy for the Pt/Mn-PANI-PPy-PGC were simultaneously observed when compared to those of Pt/Mn-PANI-PGC. These shifts in binding energy could be ascribed to electronic transfer from the deposited Pt nanoparticles to N dopants in PGC,[46, 47] likely strengthening their interaction. Also, such a transfer would affect the electronic structure of the surface Pt atoms. The resulting electron deficiency on Pt would further weaken the adsorption of O_2 during the ORR, which is potentially contributing to the improvement of catalytic activity and stability for the ORR. More STEM-EDS elemental mapping results are shown in **Figure S10** to identify the possible interactions between N and Pt, suggesting an apparent co-location of Pt and N at the nanoscale **(Figure S11)**.

Further characterization of local structure through XAS was used to provide increased understanding of the improved activity and stability of Pt/Mn-PANI-PPy-PGC in comparison to conventional Pt/C. Examination of normalized Pt-L_3 edge XANES spectra for Pt/Mn-PANI-PPy-PGC and Pt/C (**Figure 5c**) reveals that the white line intensity, sensitive to the density of unoccupied d orbitals, is higher for both Pt/Mn-PANI-PPy-PGC and Pt/C than for Pt foil, [48] indicating a higher oxidation state due to increased electron donation from Pt to N or O atoms in the vicinity. The higher white line intensity of Pt/C than Pt/Mn-PANI-PPy-PGC indicates a lower oxidation state of Pt in Pt/Mn-PANI-PPy-PGC, suggesting a possible role of N dopant in decreasing the adsorption of O-containing species on the Pt surface.

A series of EXAFS fittings were performed to characterize the local Pt structure of Pt/Mn-PANI-PPy-PGC and Pt/C using combinations of Pt-Pt, Pt-N, Pt-C and Pt-O scattering paths (**Figure 5d, Figure S12, S13,** and **S14**). Since there is no N doping in Pt/C, only Pt-Pt, Pt-C, and Pt-O scattering paths were chosen to fit its EXAFS spectrum. The results (**Table S2**) suggest that Pt-Pt and Pt-O are the major coordination interactions for Pt/C, which is consistent with previous studies.[49, 50] In contrast, results for Pt/Mn-PANI-PPy-PGC (**Table S3**) show that Pt-N is highly favoured in our catalyst, as the reduced χ^2 value (the soundness of fitting) is minimized by using the model containing only Pt-Pt and Pt-N scattering paths. The lower-coordinated Pt-Pt bonds (6.9 compared to 12 in fully coordinated Pt bulk, **Table S3**) is also indicative of Pt nanoparticles, [51, 52] which is consistent with TEM images. In addition, the possibility of Pt-O and Pt-C coordination was investigated by performing several independent EXAFS fittings, which show that Pt-O coordination is also possible, while Pt-C coordination does not appear significant **(Figure S14, Table S3)**. Although it is hard to completely exclude the existence of Pt-O, the comparison of EXAFS fitting results for Pt/Mn-PANI-PPy-PGC and Pt/C suggest that Pt-N coordination predominates in Pt/Mn-PANI-PPy-PGC. This interpretation is further supported by the difference in the white line intensity in XANES spectra. As shown in **Figure 5c**, the white line intensity of Pt in Pt/C is higher than that of Pt in Pt/Mn-PANI-PPy-PGC, which can be attributed to decreased filling of the *d* band in Pt/C due to the higher electronegativity of oxygen relative to nitrogen. These XANES and EXAFS fitting results collectively suggest a high likelihood of Pt-N interaction in Pt/Mn-PANI-PPy-PGC (**Figure 5d**), in agreement with the XPS and the STEM-EDS elemental mapping results. This Pt-N interaction appears to contribute to the increased stability and activity of our catalyst compared to non-doped commercial Pt/C catalysts.

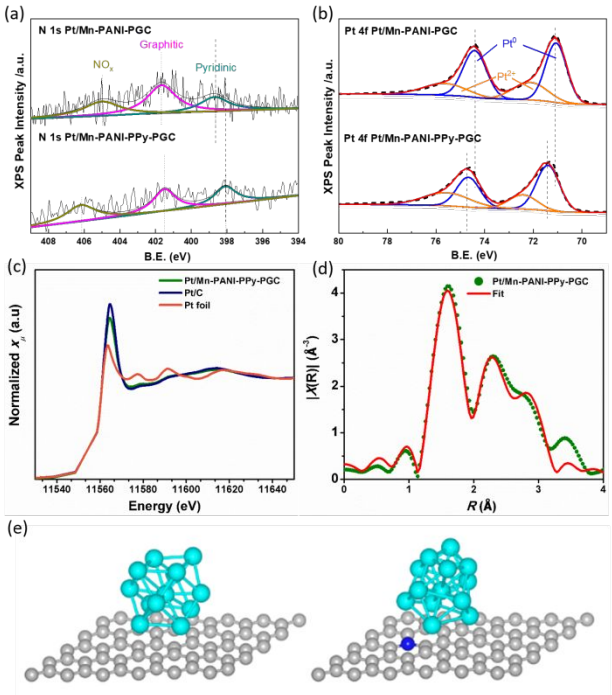

Figure 5. High-resolution XPS **(a)** N1s and **(b)** Pt 4f spectra of Pt catalysts supported on Mn-PANI-PGC and Mn-PANI-PPy-PGC; XANES and EXAFS spectra of Pt/Mn-PANI-PPy-PGC and Pt/C: **(c)** Comparison of Pt L3-edge XANES spectra for Pt/Mn-PANI-PPy-PGC, Pt/C and Pt foil, **(d)** Fourier-transformed magnitudes of Pt L3-edge EXAFS spectra in R space for Pt/Mn-PANI-PPy-PGC fitted with Pt-Pt and Pt-N scattering paths. (**e**) Optimized atomistic structures (side view) of a thirteen-Pt-atom cluster adsorbed on a pristine graphene layer (left) and an N-doped graphene layer (right). In the figure, the gray, cyan, and blue balls represent carbon, platinum, and nitrogen atoms, respectively.

Density functional theory (DFT) calculations were performed to provide atomistic/electronic insights into the effects of N doping on the interaction between Pt and carbon supports. A model system consisting of a single Pt atom and a graphene layer with or without graphitic N doping was used in the calculations. The DFT optimized atomistic structures of various possible adsorption configurations and the corresponding binding energies of a Pt atom on the graphene are shown in **Figures 5e, S15,** and **S16**. The calculated binding energies are negative for all the configurations, indicating that it is energetically favorable for a single Pt atom to be adsorbed on a graphene layer. For both pristine and N-doped graphene layers, the bridge site (right above a C-C bond) was found to be the most favorable adsorption site of a Pt atom on graphene. Moreover, DFT results showed that the bridge site adjacent to the N dopant was more attractive to the Pt atom as compared to those in the pristine graphene layer. The binding energy difference ΔE_b is calculated to be -0.40 eV, suggesting a strengthening effect somewhat stronger than the previously reported value of -0.23 eV.[53] To further verify the anchoring effect of N dopant, we evaluated the same strengthening parameter for a cuboctahedral Pt_{13} cluster adsorbed on the graphene layer, for which optimized structures are shown in **Figure S17**. The N-doped graphene was found to bind the Pt_{13} cluster more strongly than pristine graphene, with ΔE_b calculated to be -0.46 eV. Hence, these DFT predictions support our experimental observations and spectroscopy results from both XPS and XAS, demonstrating how N dopant in the carbon support can improve the stability of Pt/C catalysts by binding Pt particles more strongly to the support.

Point defects in graphene, such as graphitic N, are known to modify the local electronic structure. The charge density difference of an N-doped graphene layer is plotted in **Figure S18a**. Nitrogen is more electronegative than carbon. Consequently, some amount of electron density is transferred from the adjacent C atoms to the N dopant, as can be observed in **Figure S18a**. This leads to a positively charged region around C atoms and negatively charged region around the N dopant. Since the Pt_{13} cluster acts as an electron donor (**Figure S18b** and **c**), these positively charged C atoms would increase the electron transfer from the Pt_{13} cluster to the N-doped graphene layer indirectly, strengthening the interaction with the Pt_{13} cluster. [54] In this way, the binding strength between Pt clusters and the N-doped graphene would be enhanced.

2.3 Key factors to stability enhancement of PGCs

To fully elucidate the key factors to the encouraging stability enhancement observed with the PGC support, we systematically studied the synthetic chemistry of PGCs and assessed correlations among synthesis, structure, and properties. The parameters examined during the synthesis include carbonization temperature, type of metals (Fe, Co, Ni, or Mn) as catalysts, heat treatment temperature (800-1100°C), duration (1 to 3 hours), and the post annealing treatment.

As the first heat treatment temperature can influence graphitization and morphology of carbon, we compared the stability of PANI-Mn derived PGC-supported Pt catalysts as a function of heating temperature from 900°C to 1100°C (**Figure S19)**. Enhanced stability was observed with increasing heat treatment temperature up to 1100°C, in good agreement with the increased graphitization observed in Raman spectra (Figure 2a). To study the role of Mn in catalyzing the graphitization process, we also compared the stability of Pt catalysts supported by Fe, Co, and Ni derived hydrogel carbon (**Figure S20)**, which were synthesized by identical methods. Only Mn provided high stability by producing highly graphitized carbon, in agreement with Raman analysis (Figure S2)**.** The unique role of Mn in catalyzing the graphitization process is also verified in our previous work to develop stable non-Pt catalysts.[55-57] This also confirms the important role of graphitization in determining the stability of PGC-supported Pt catalysts. Under even higher potential range cycling (1.0-1.6 V), PGC-supported Pt catalysts are still able to maintain good performance for 10,000 cycles. While 104 mV $E_{1/2}$ loss was observed with the TEC10V20E, the best performing Pt/Mn-PANI-PPy-PGC only lost 24 mV under identical cycling conditions (**Figure S21**).

Post annealing treatment at 800°C was applied to further stabilize the PGC-supported Pt catalysts. After post annealing treatment, the activity of Pt/Mn-PANI-PPy-PGC was improved

slightly (**Figure S22**), especially in the kinetic range. Importantly, the stability was enhanced significantly. A careful comparison of mapping images between **Figure S10** and **Figure S23** suggests that these improvements are caused by enhanced interactions between Pt and support induced by N doping. As identified by using in-situ HR-TEM, the slightly increased size of Pt nanoparticles from 3 to 5 nm during the annealing may also further stabilize the Pt catalysts.

2.3 Catalyst activity and stability for the ORR

Electrochemical performance of the PGC-supported Pt and various commercial Pt/C catalysts, including TEC10V20E (Vulcan support), TEC10EA20E (graphitized carbon support), and TEC10E20E (high-surface-area carbon black), were measured in 0.1 M $HClO_4$ solution using a rotating disk electrode (RDE) for the ORR (**Figure 6a-c**). Except for the TEC10E20E catalyst, which is supported on high-surface area carbon with highest electrochemical active surface area (ECSA) of Pt (83.7 m^2/g), the Pt/PGC catalyst shows enhanced kinetic activity demonstrated by the positive shift of half-wave potential ($E_{1/2}$) when compared to TEC10V20E and TEC10EA20E. This is in good agreement with the increased ECSA of Pt deposited on PGC up to 67.2 m^2/g_{Pt} vs TEC10V20E (55.1 m^2/g_{Pt}) and TEC10EA20E (48.4 m^2/g_{Pt})(**Figure 6b**). The increased ECSA of the Pt/PGC catalyst is likely due to more uniform dispersion of Pt nanoparticles on the PGC support, which is due to its higher BET surface area and unique hierarchical porosity shown in **Figure S24.** A detailed comparison of various Pt catalysts in terms of their ECSA and Pt particle sizes was tabulated in **Table S4**. It should be noted that the measured limiting current densities for the various Pt/C catalysts are very close to the theoretical value calculated at a rotation speed of 1600 rpm. The mass activity, calculated from kinetic current densities with IR correction at 0.9 V, is listed in **Figure 6c**. In a good agreement with the measurement of $E_{1/2}$, TEC10E20E exhibits the highest value around 500 mA/μg_{Pt}, followed by the Pt/PGC (300 mA/μg_{Pt}), TEC10V20E (210 mA/μg_{Pt}), and TEC10EA20E (190 mA/μg_{Pt}) catalysts. The lower mass activity of Pt/PGC relative to high-surface area TEC10E20E is probably due to larger Pt particle size and lower ECSA. However, the Pt/PGC specific activity is comparable to that of TEC10E20E, indicating a high intrinsic ORR activity. The comprehensive comparison of all studied Pt/C catalysts in terms of their steady-state polarization plots, ECSAs, mass activity, and specific activity demonstrate the favorable properties of PGC in enabling good ORR kinetics.

Accelerated stress tests (ASTs) were conducted on RDEs with a Pt loading of 20 $\mu g_{Pt}/cm^2$ by cycling the potentials in both low (0.6-1.0 V, 50 mV/s) and high (1.0-1.5 V, 500 mV/s) potential ranges to evaluate degradation of the Pt nanoparticles and the carbon support, respectively. To simulate the harsh environment in a fuel cell, we increased electrolyte temperature to 60°C to study the carbon corrosion in high potential ranges. **Figure 6d-f** compare the carbon support stability after 10,000 cycles from 1.0 to 1.5 V for various Pt catalysts. While 46 mV $E_{1/2}$ loss was measured with the Vulcan carbon-based TEC10V20E, only 17 mV $E_{1/2}$ loss was observed with both Pt/PGC and the graphitized TEC10EA20E catalysts. This indicates that, similar to the highly graphitized carbon support, the PGC can provide excellent carbon support stability under harsh oxidative conditions. This outstanding carbon corrosion resistance for both PGC and highly graphitized carbon is in agreement with the Raman spectra in **Figure S25**. In addition, **Figure S26** further compares the catalytic stability after 30,000 cycles at low potential cycles (0.6-1.0 V) to study the activity loss due to possible Pt particle agglomeration. Under this AST, the enhanced Pt catalyst stability on the PGC support (31 mV loss) was apparent compared to Vulcan, high-surface-area carbon and graphitized carbon supported Pt catalysts with losses of $E_{1/2}$ of 64, 29 and 36 mV, respectively. The comparison also suggests that PGC provides strong interactions between Pt nanoparticle and support to hinder Pt agglomeration, likely due to the promotional role of N doping and the unique hierarchical porosity. A comprehensive comparison of stability tests for each of the Pt catalysts is provided in **Figure S27**. Compared to the Vulcan support, the PGC provides significant stability improvement for both Pt nanoparticles and support. As for the highly graphitized carbon in the TEC10EA20E catalyst, even though they have comparable stability during high potential cycles, the PGC provides much higher Pt ECSA and higher ORR activity.

TEM and STEM images of the Pt/Mn-PANI-PPy-PGC catalyst after various ASTs, including both high and low potential cycling, are shown in **Figure S28**. Before the ASTs, the mean Pt particle size was about 5.6 nm (**Figure S29a**). A wide distribution of Pt particle size may result from the post annealing treatment. It should be noted that the mean Pt particle size for the Pt/Mn-PANI-PPy-PGC without post treatment is about 3.8 nm (**Figure S23)**, indicating that post treatment indeed increases the particle size (Figure 4d), which benefits the catalyst stability **(Figure S22)**. While high potential ASTs lead to an increase of Pt particle size slightly from 5.6 to 7.2 nm (**Figure S28, S29**) the graphitic carbon structure appeared unchanged. Due to the strengthened Pt and support interaction, Pt particle size distribution is nearly retained after low-potential ASTs except for the formation of some large particles up to 8.0-8.5 nm **(Figure S29)**. The Pt particles remained well dispersed on the graphitic carbon structure **(Figure S28c)**, indicating that this unique structure and morphology of PGC support was able to stabilize Pt particles. For a comparison, we used the same method to deposit Pt on nitrogen-doped multi-walled carbon nanotubes (MWCNTs), which are representative of graphitized carbon material used in previous research. The poor stability of Pt/MWCNT shown in **Figure S30** suggests that, in addition to high graphitization degree, the unique porosity of PGC supports derived from polymer hydrogel provides further stabilization of Pt nanoparticles. In addition, after low potential ASTs, the mean Pt particle size remained nearly unchanged at 5.9 nm. Unlike the low surface area Vulcan carbon (250 m^2/g), the enhancement of stability might be ascribed to the structural features of PGC, *i.e*. high surface area and porosity, which hinder the Pt growth. In particular, the highly folded graphitic structure might limit the movement of Pt particles.[58] Thus, PGC with appropriate porosity, folded morphology, and high degree of graphitization enhances stability of Pt nanoparticles during the low potential

range AST. Elemental mapping and overall morphologies of Pt/Mn-PANI-PPy-PGC after various ASTs are depicted in **Figure S31**, showing that the carbon structures and the nitrogen doping are retained, and Pt nanoparticle growth is insignificant after low potential cycling.

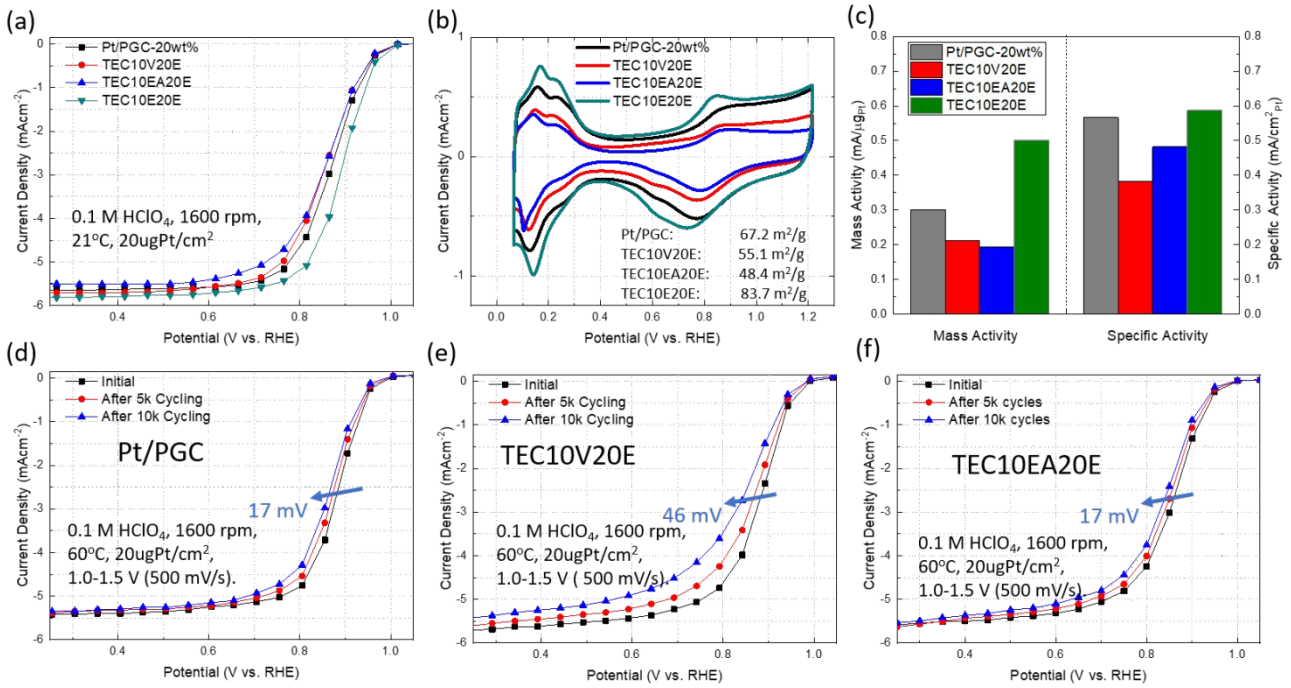

Figure 6. (a) ORR polarization plots for Pt/PGC catalysts and various commercial Pt/C catalysts, **(b)** the corresponding CV plots and the corresponding ECSA, and **(c)** the corresponding mass activities and specific activities at 0.9 V after IR correction; RDE potential cycling stability tests for **(d)** Pt/Mn-PANI-PPy-PGC, **(e)** TEC10V20E and **(f)** TEC10EA20E during high potential range (1.0-1.5V).

2.4 Fuel cell stability evaluation and carbon corrosion analysis

Given the significant difference of conditions between traditional RDE and fuel cells, the PGC-supported Pt catalysts were carefully evaluated in MEAs under a real fuel cell environment and compared with commercially available Pt/C catalysts. Polarization performance was measured in H_2/air, and ASTs were applied under H_2/N_2 in both high (1.0-1.5 V) and low (0.6-0.95 V) potential ranges at 80°C and 100% RH. In addition to slightly enhanced initial fuel cell performance, the PGC-supported Pt catalyst, especially the Pt/Mn-PANI-PPy-PGC, exhibited significantly enhanced stability. In particular, after 5000 cycles from 1.0-1.5 V, the commercial Pt/C cathode (TEC10V20E) suffers from a serious degradation at a current density of 1.5 A/cm^2 (**Figure 7a**) In contrast, the Pt/Mn-PANI-PPy-PGC catalyst demonstrated exceptionally high stability, with only 9 mV loss (**Figure 7b**), easily meeting the DOE target of less than 30 mV loss. The performance losses summarized in **Figure S32** demonstrate the durability advantages of the Mn-PANI-PPy-PGC support in fuel cells. Carbon corrosion analysis shown in **Figure 7c** demonstrates that carbon loss from TEC10V20E is almost five times higher than that of Pt/Mn-PANI-PPy-PGC under the same conditions. This is also in good agreement with the ECSA analysis carried out under fuel cell conditions (**Figure 7d**), indicating a much smaller loss of ECSA for Pt/Mn-PANI-PPy-PGC (34.4%) relative to TEC10V20E (74.4%). The Pt/PGC catalyst is also superior to the highly graphitized carbon –based TEC10EA20E tested by Borup *et al*., at Los Alamos National Laboratory in **Figure S33**.[59] These results demonstrate the excellent resistance to carbon corrosion and the high durability of Mn-PANI-PPy-PGC support, which significantly surpasses that of commercial carbons. For the low potential (0.6-0.95 V) range cycling, the performance of Pt/Mn-PANI-PPy-PGC is retained well, especially in the kinetic range when compared to other commercially available Pt/C catalysts (**Figure S34**), which is in agreement with RDE testing results. The fuel cell testing results further confirm the significantly enhanced stability due to the use of the Mn-PANI-PPy hydrogel-derived carbon. **Table S5** further provides a detailed comparison of the unique properties and performance of the newly developed PGC with commercial Pt/C catalysts based on various carbon supports for fuel cell applications.

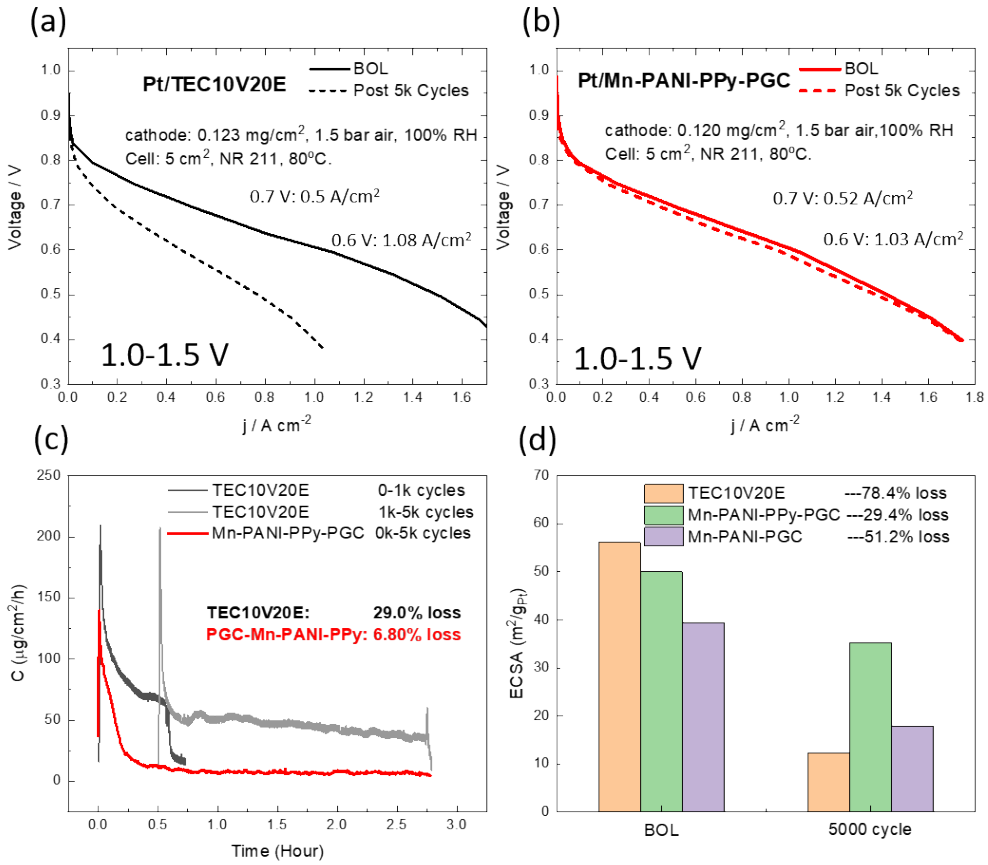

Figure 7. Fuel cell performance of **(b)** Pt/Mn-PANI-PPy-PGC with a comparison with **(a)** a commercial Pt/C (TEC10V20E) during high potential ASTs; **(c)** corresponding comparison of carbon loss during those ASTs (total carbon content during testing: TEC10V20E - 0.38 mg/cm^2, Pt/Mn-PANI-PPy-PGC - 0.43 mg/cm^2, Pt/Mn-PANI-PGC - 0.52 mg/cm^2); **(d)** ECSA analysis during corresponding ASTs in MEAs.

3. Conclusion

To address the grand stability challenges of Pt/C catalysts for fuel cell applications, we developed a highly stable and favorable carbon support for Pt nanoparticles based on a polymer composite hydrogel precursor consisting of PANI and PPy as carbon/nitrogen sources in combination with Mn as a graphitization catalyst. The stability enhancement was carefully and comprehensively evaluated in both aqueous acidic electrolyte-based RDE and real fuel cell conditions by using a variety of accelerated stress test protocols recommended by U.S. DOE. The Mn-PANI-PPy hydrogel-derived carbon provides high graphitization degree and good morphology (*e.g.*, sufficient surface area, and porosity), enabling exceptional catalytic stability. Among many important findings, we discovered the importance of binary PANI and PPy polymer hydrogel and the unique role of Mn during the carbonization, which yield dramatically increased degree of graphitization and favorable hierarchical pore morphology for increased Pt utilization and strengthened metal-support interactions. Compared to other possible metals (*e.g.*, Fe, Co, or Ni) as catalysts during the graphitization process, Mn was found to play an indispensable role in forming the highest degree of graphitization at optimized temperature and duration of the carbonization process. In addition to their excellent electrochemical properties as catalyst supports, these PGC materials are more suitable for low-cost manufacturing, since temperatures of only 1100°C are needed, compared with heat treatments up to 3000°C required for conventional graphitized carbons. In-situ HR-TEM and STEM further reveal that Mn is able to be uniformly dispersed into the hydrogel precursors at high temperature and effectively catalyze the graphitization process. Unlike other transition metals, Mn itself does not alloy with Pt and can be removed during the subsequent acidic leaching treatment. Post annealing treatment was found to strengthen Pt-support interactions, further enhancing stability. Importantly, the promotional role of nitrogen doping in facilitating the activity and stability enhancement was validated through high-resolution microscopy and X-ray absorption spectra in combination with theoretical DFT calculations. A high likelihood of Pt-N interaction is due to the possible electron transfer from Pt nanoparticles to N dopant in carbon support, leading to strengthened interactions of metal and supports by binding Pt atoms strongly to the graphitic N, while electron transfer from C to adjacent N atoms results in stronger interaction between Pt and C.

The high surface area, abundant porosity, and N doping present in PGCs create a favorable environment to disperse Pt nanoparticles and prevent agglomeration. Meanwhile, the remarkably improved degree of graphitization enhances carbon corrosion resistance in fuel cell cathodes. The well balanced porosity and graphitization of PGCs provide unique structural and morphological advantages to produce highly active and stable carbon supported Pt catalysts for PEMFCs. This new type of PGC--supported Pt catalyst significantly surpasses the state-of-the-art Pt/C and provides exceptionally enhanced stability with minimized carbon loss at high potentials. The advanced PGC represents a new class of carbon for fuel cells with extraordinarily enhanced durability

Acknowledgements

This work was financially supported by start-up funding from the University at Buffalo, SUNY (G. Wu) and U.S. DOE-EERE Fuel Cell Technologies Office (Gang Wu and J.S.S.). Z. F. thanks the start-up support from Oregon State University. Electron microscopy research was conducted at the Center for Functional Nanomaterials at Brookhaven National Laboratory under Contract DE-SC0012704, which is DOE Office of Science User Facilities. XAS measurements were done at 20-BM at Advanced Photon Source (APS) of Argonne National Laboratory (ANL). The use of APS of ANL is supported by DOE under Contract Number DE-AC02-06CH11357. G.F. Wang gratefully acknowledges the computational resources provided by the computer facility at Center for Simulation and Modeling of the University of Pittsburgh and at the Extreme Science and Engineering Discovery Environment (XSEDE), which is supported by National Science Foundation grant number ACI-1053575.

References

1. Y. Shao, J. Liu, Y. Wang and Y. Lin, *Journal of Materials Chemistry*, 2009, **19**, 46-59.
2. J. Zhou, X. Zhou, X. Sun, R. Li, M. Murphy, Z. Ding, X. Sun and T.-K. Sham, *Chemical physics letters*, 2007, **437**, 229-232.
3. X. Yu and S. Ye, *Journal of Power Sources*, 2007, **172**, 145-154.
4. Y.-J. Wang, N. Zhao, B. Fang, H. Li, X. T. Bi and H. Wang, *Chemical reviews*, 2015, **115**, 3433-3467.
5. J. Wang, G. Yin, Y. Shao, Z. Wang and Y. Gao, *The Journal of Physical Chemistry C*, 2008, **112**, 5784-5789.
6. D. Stevens, M. Hicks, G. Haugen and J. Dahn, *Journal of the Electrochemical Society*, 2005, **152**, A2309-A2315.
7. J. Guo, G. Sun, Q. Wang, G. Wang, Z. Zhou, S. Tang, L. Jiang, B. Zhou and Q. Xin, *Carbon*, 2006, **44**, 152-157.
8. G. Wu, Y.-S. Chen and B.-Q. Xu, *Electrochemistry Communications*, 2005, **7**, 1237-1243.
9. Q. Li, H. Pan, D. Higgins, R. Cao, G. Zhang, H. Lv, K. Wu, J. Cho and G. Wu, *Small*, 2015, **11**, 1443-1452.
10. Y. Shao, G. Yin and Y. Gao, *Journal of Power Sources*, 2007, **171**, 558-566.
11. M. Chen, S. Hwang, J. Li, S. Karakalos, K. Chen, Y. He, S. Mukherjee, D. Su and G. Wu, *Nanoscale*, 2018, **10**, 17318-17326.
12. H. Guo, W. He, Y. Lu and X. Zhang, *Carbon*, 2015, **92**, 133-141.
13. X.-L. Wu, T. Wen, H.-L. Guo, S. Yang, X. Wang and A.-W. Xu, *ACS nano*, 2013, **7**, 3589-3597.
14. Z. Qiao, H. Zhang, S. Karakalos, S. Hwang, J. Xue, M. Chen, D. Su and G. Wu, *Applied Catalysis B: Environmental*, 2017, **219**, 629-639.
15. C. Zhu, S. Fu, J. Song, Q. Shi, D. Su, M. H. Engelhard, X. Li, D. Xiao, D. Li, L. Estevez, D. Du and Y. Lin, *Small*, 2017, DOI: 10.1002/smll.201603407, DOI: 10.1002/smll.201603407.
16. Z.-S. Wu, S. Yang, Y. Sun, K. Parvez, X. Feng and K. Müllen, *Journal of the American Chemical Society*, 2012, **134**, 9082-9085.
17. B. You, P. Yin, J. Zhang, D. He, G. Chen, F. Kang, H. Wang, Z. Deng and Y. Li, *Scientific reports*, 2015, **5**, 11739.
18. G. Wu, K. L. More, C. M. Johnston and P. Zelenay, *Science*, 2011, **332**, 443-447.
19. A. Q. Zhang, Y. Zhang, L. Z. Wang and X. F. Li, *Polymer Composites*, 2011, **32**, 1-5.
20. H. Mi, X. Zhang, X. Ye and S. Yang, *Journal of Power Sources*, 2008, **176**, 403-409.
21. N. H. Xie, X. H. Yan and B. Q. Xu, *ChemSusChem*, 2016, **9**, 2301-2306.
22. P. Xu, X. Han, C. Wang, B. Zhang, X. Wang and H. L. Wang, *Macromolecular Rapid Communications*, 2008, **29**, 1392-1397.
23. Y. Zhou, K. Neyerlin, T. S. Olson, S. Pylypenko, J. Bult, H. N. Dinh, T. Gennett, Z. Shao and R. O'Hayre, *Energy & Environmental Science*, 2010, **3**, 1437-1446.
24. S. Maldonado and K. J. Stevenson, *The Journal of Physical Chemistry B*, 2005, **109**, 4707-4716.
25. Y. Shao, J. Sui, G. Yin and Y. Gao, *Applied Catalysis B: Environmental*, 2008, **79**, 89-99.
26. A. Ōya and S. Ōtani, *Carbon*, 1979, **17**, 131-137.
27. G. Wu, K. Artyushkova, M. Ferrandon, A. J. Kropf, D. Myers and P. Zelenay, *Ecs Transactions*, 2009, **25**, 1299-1311.
28. D. Banham, S. Ye, K. Pei, J.-i. Ozaki, T. Kishimoto and Y. Imashiro, *Journal of Power Sources*, 2015, **285**, 334-348.
29. T. H. Ko, *Journal of Applied Polymer Science*, 1996, **59**, 577-580.
30. F. Maldonado-Hódar, C. Moreno-Castilla, J. Rivera-Utrilla, Y. Hanzawa and Y. Yamada, *Langmuir*, 2000, **16**, 4367-4373.
31. R. Andrews, D. Jacques, D. Qian and E. Dickey, *Carbon*, 2001, **39**, 1681-1687.
32. G. Wu, C. M. Johnston, N. H. Mack, K. Artyushkova, M. Ferrandon, M. Nelson, J. S. Lezama-Pacheco, S. D. Conradson, K. L. More and D. J. Myers, *Journal of Materials Chemistry*, 2011, **21**, 11392-11405.
33. J.-M. Vallerot, X. Bourrat, A. Mouchon and G. Chollon, *Carbon*, 2006, **44**, 1833-1844.
34. N. McEvoy, N. Peltekis, S. Kumar, E. Rezvani, H. Nolan, G. P. Keeley, W. J. Blau and G. S. Duesberg, *Carbon*, 2012, **50**, 1216-1226.
35. A. C. Ferrari, *Solid state communications*, 2007, **143**, 47-57.

36. S. Pisana, M. Lazzeri, C. Casiraghi, K. S. Novoselov, A. K. Geim, A. C. Ferrari and F. Mauri, *Nature materials*, 2007, **6**, 198.
37. J. Yan, Y. Zhang, P. Kim and A. Pinczuk, *Physical review letters*, 2007, **98**, 166802.
38. W. Bacsa, J. Lannin, D. Pappas and J. Cuomo, *Physical Review B*, 1993, **47**, 10931.
39. T. Jawhari, A. Roid and J. Casado, *Carbon*, 1995, **33**, 1561-1565.
40. R. Vidano, D. Fischbach, L. Willis and T. Loehr, *Solid State Communications*, 1981, **39**, 341-344.
41. D. R. Rolison, *Science*, 2003, **299**, 1698-1701.
42. G. Wu, N. H. Mack, W. Gao, S. Ma, R. Zhong, J. Han, J. K. Baldwin and P. Zelenay, *ACS Nano*, 2012, **6**, 9764-9776.
43. G. Wu, M. Nelson, S. Ma, H. Meng, G. Cui and P. K. Shen, *Carbon*, 2011, **49**, 3972-3982.
44. Q. Li, G. Wu, D. A. Cullen, K. L. More, N. H. Mack, H. T. Chung and P. Zelenay, *ACS Catalysis*, 2014, **4**, 3193-3200.
45. S.-I. Hirano, T. Yogo, H. Suzuki and S. Naka, *Journal of Materials Science*, 1983, **18**, 2811-2816.
46. L. Qiu, F. Liu, L. Zhao, W. Yang and J. Yao, *Langmuir*, 2006, **22**, 4480-4482.
47. L. Guo, W.-J. Jiang, Y. Zhang, J.-S. Hu, Z.-D. Wei and L.-J. Wan, *ACS Catalysis*, 2015, **5**, 2903-2909.
48. H. Zhang, P. An, W. Zhou, B. Y. Guan, P. Zhang, J. Dong and X. W. D. Lou, *Science advances*, 2018, **4**, eaao6657.
49. K. Zhang, W. Yang, C. Ma, Y. Wang, C. Sun, Y. Chen, P. Duchesne, J. Zhou, J. Wang and Y. Hu, *NPG Asia Materials*, 2015, **7**, e153.
50. J. N. Tiwari, S. Sultan, C. W. Myung, T. Yoon, N. Li, M. Ha, A. M. Harzandi, H. J. Park, D. Y. Kim and S. S. Chandrasekaran, *Nature Energy*, 2018, **3**, 773.
51. Z. Weng, Y. Wu, M. Wang, J. Jiang, K. Yang, S. Huo, X.-F. Wang, Q. Ma, G. W. Brudvig and V. S. Batista, *Nature communications*, 2018, **9**, 415.
52. A. I. Frenkel, A. Yevick, C. Cooper and R. Vasic, *Annual Review of Analytical Chemistry*, 2011, **4**, 23-39.
53. T. Holme, Y. K. Zhou, R. Pasquarelli and R. O'Hayre, *Phys Chem Chem Phys*, 2010, **12**, 9461-9468.
54. H. B. Shi, S. M. Auerbach and A. Ramasubramaniam, *J Phys Chem C*, 2016, **120**, 11899-11909.
55. X. Wang, Q. Li, H. Pan, Y. Lin, Y. Ke, H. Sheng, M. T. Swihart and G. Wu, *Nanoscale*, 2015, **7**, 20290-20298.
56. S. Gupta, S. Zhao, X. X. Wang, S. Hwang, S. Karakalos, S. V. Devaguptapu, S. Mukherjee, D. Su, H. Xu and G. Wu, *ACS Catalysis*, 2017, **7**, 8386-8393.
57. J. Li, M. Chen, D. A. Cullen, S. Hwang, M. Wang, B. Li, K. Liu, S. Karakalos, M. Lucero, H. Zhang, C. Lei, H. Xu, G. E. Sterbinsky, Z. Feng, D. Su, K. L. More, G. Wang, Z. Wang and G. Wu, *Nature Catalysis*, 2018, **1**, 935-945.
58. Y. Xin, J.-g. Liu, Y. Zhou, W. Liu, J. Gao, Y. Xie, Y. Yin and Z. Zou, *Journal of Power Sources*, 2011, **196**, 1012-1018.
59. R. L. Borup, R. Mukundan, D. Spernjak, K. C. Rau, D. A. Langlois and D. J. Torraco, *Durability Improvements through Degradation Mechanism Studies*, 2014 U.S. DOE Hydrogen and Fuel Cell Technology Annual Merit Review Proceeding.

Graphical abstract